Springer

Available online at https://link.springer.com/journal/42241
http://www.jhydrodynamics.com
Journal of Hydrodynamics, 2019, 31(1): 152-168
https://doi.org/10.1007/s42241-018-0145-z

Hydrodynamic pressure on concrete face rockfill dams subjected to earthquakes *

Zhong-zhi Fu[1, 2], Sheng-shui Chen[1, 2], Guo-ying Li[1, 2]
1. *Geotechnical Engineering Department, Nanjing Hydraulic Research Institute, Nanjing 210024, China*
2. *Key Laboratory of Failure Mechanism and Safety Control Techniques of Earth-Rock Dams, Ministry of Water Resource, Nanjing 210029, China*

(Received June 24, 2016, Revised November 27, 2016, Accepted December 5, 2016, Published online November 30, 2018)

Abstract: The hydrodynamic pressure is an important load on concrete face rockfill dams (CFRDs) subjected to earthquakes, the influence of which, however, is not clear as compared with that in concrete dams. In this paper, the coupling effect between the CFRDs and the reservoir water is studied based on two-dimensional finite element simulations by using a verified procedure. It is found that neglecting the solid-fluid coupling effect not only results in an overestimation of the acceleration response within the rockfill materials but also makes an overestimation of the dynamical stresses in the concrete slabs. For a reliable seismic response analysis of the CFRDs, therefore, the hydrodynamic pressure should be taken into account, particularly when the dam is subjected to a simultaneous excitation in both horizontal and vertical directions. Numerical results show, however, that the compressibility of the water can be safely neglected in the seismic response analyses of the CFRDs even when the dam is as high as 300 m, except when the excitation is quite abundant in high frequency contents.

Key words: Concrete face rockfill dam, hydrodynamic pressure, seismic response, earthquake

Introduction

A concrete face rockfill dam (CFRD) is a water retaining infrastructure playing often a multiple role of the flood control, the agricultural irrigation, the power generation, the environmental protection and others. This type of dams is considered inherently of high resistance to earthquakes because of the use of coarse rockfill materials and the low probability of the pore pressure generation. In spite of their capability of maintaining an overall stability during earthquakes, serious damage can always be observed in the CFRDs after major earthquakes, such as the compressive and tensile failure of concrete slabs, a considerable settlement of the dam and the cracks along different directions at the crest[1]. The seismic response analysis, therefore, is important in designing CFRDs in the regions of high seismicity. An in-depth understanding of the dynamic behavior of dam materials and the dynamic loads applied to the structures during earthquakes is desirable for this purpose.

An important load on the water-retaining structures excited by earthquakes is the hydrodynamic pressure upon the solid-fluid interface[2-3]. Early studies were focused on deriving an analytical solution of the hydrodynamic pressure applied on a rigid vertical surface due to a horizontal acceleration. The appealing concept of the added mass of the fluid could be derived from such a solution[2, 4]. The hydrodynamic pressure upon the sloping dams was also studied mathematically and by the electric analog. In these early studies, the dam was assumed to be rigid and the viscosity and the surface waves as well as the nonlinear convective acceleration in the water were generally neglected. The influence of the flexibility of the dams on the hydrodynamic pressure was studied[5-6]. It was found that the compressibility of the reservoir water has an insignificant effect on the earthquake excited dam response provided that the dam is flexible enough as compared with the reservoir system. Because of the complexity of the problem,

* Project supported by the National Key Research and Development Program of China (Grant No. 2017YFC0404806), the National Natural Science Foundation of China (Grant Nos. 51779152, 51539006).
Biography: Zhong-zhi Fu (1984-), Male, Ph. D., Senior Engineer
Corresponding author: Zhong-zhi Fu,
E-mail: fu_zhongzhi@yahoo.com

analytical solutions can be obtained only in cases where the geometries and boundary conditions are regular and simple.

The progress of computational and numerical techniques, exemplified by the finite element method (FEM), the finite difference method (FDM) and the boundary element method (BEM), largely removes the restriction on the geometry and boundary conditions. The presence of the surface gravity waves, the compressibility and the cavitation of the reservoir water, the convective acceleration, the opening and closure of the contraction joints and the conditions on the truncated boundaries could be considered flexibly, and their influences on the hydrodynamic pressure as well as the seismic response of structures can be evaluated effectively[7-10]. These numerical studies were mostly oriented to the seismic response of concrete dams, and the following conclusions could be summarized:

(1) Neglecting the water compressibility (and thus the reservoir boundary absorption) may result in a considerable underestimation or overestimation of the dynamic stresses in arch dams, depending on the frequency characteristics of the ground motion as well as the vibration periods of the dam[5-6].

(2) The effects of the surface wave and the convective acceleration on the hydrodynamic pressure could increase the hydrodynamic pressure by 10%, as compared with a linear analysis with the neglect of these effects[8], therefore a complete three-dimensional nonlinear analysis is important in designing an arch dam. Other factors like the opening of the contraction joints and the radiation damping of the foundation rock should also be considered properly[6, 10].

(3) The cavitation of the fluid and the nonlinear structural behavior can interact to affect the response of a coupled system. However, the cavitation appears to have a very small and negligible effect on the maximum displacements and the stresses of gravity dams[9].

Compared with abundant studies of hydrodynamic pressure problems for concrete dams, the hydrodynamic pressure upon concrete slabs in the CFRDs attracted considerably less attentions in the past years. Bureau et al.[11] conducted a series of equivalent-linear finite element simulations to study the effect of the fluid-dam interaction and to estimate the axial forces and the bending moments on the concrete slabs. They concluded that the hydrodynamic effects can be safely ignored in estimating the seismic response of the CFRDs. However, their conclusion was based on a hypothetical CFRD with a height of 100 m, and it is not clear whether this conclusion is appropriate for higher CFRDs. Employing a Lagrangian description of the fluid system, Bayraktar et al.[12] studied the seismic response of a CFRD including the dam and reservoir interaction. The contacting behavior between the concrete slabs and the reservoir water was modeled by short and almost axially rigid truss elements in the normal direction of the concrete slabs. However, the magnitude of the hydrodynamic pressure and its effect on the dam response were not explicitly addressed. In fact, it is a common practice to neglect the hydrodynamic pressure on concrete slabs or to evaluate the pressure by using some approximations [13-16]. It is not clear whether such a simplification results in an overall overestimation or underestimation of the hydrodynamic pressure and what is the consequent influence on the response of the CFRDs.

The aim of the present paper is to clarify the above points so as to provide a confidence or a caution in studying the seismic response of the CFRDs by simplified methods. The governing equations of the solid and fluid coupling system are revisited and the equivalent algebraic equations as well as the solution strategy are presented. A series of two-dimensional analyses are conducted to study the effects of the fluid compressibility, the dam height and stiffness and the frequency of the input ground accelerations. A two-dimensional plane strain analysis is preferred in this study because of the simplicity in interpreting the obtained results.

1. Formulations

1.1 *Governing equations*

Since the pore pressure seldom builds up within rockfill materials when being shook by earthquakes, the dynamic equilibrium equation for the solid system can be expressed simply using the total stress tensor, i.e.

$$\rho_s \ddot{\boldsymbol{u}} + \alpha \rho_s \dot{\boldsymbol{u}} + \nabla \cdot \boldsymbol{\sigma} = -\rho_s \ddot{\boldsymbol{u}}_g \tag{1}$$

where ρ_s stands for the material density, $\ddot{\boldsymbol{u}}_g$ denotes the ground acceleration and $\ddot{\boldsymbol{u}}$ the relative acceleration to the ground, $\nabla \cdot \boldsymbol{\sigma}$ denotes the divergence of the dynamic stress tensor, $\boldsymbol{\sigma}$, ∇ is the gradient operator. The second term on the left hand side of Eq. (1) reflects the damping force, which is proportional to the relative velocity, $\dot{\boldsymbol{u}}$, with a coefficient α.

The dynamic stress could be seen as a function of the dynamic strain in the framework of visco-elasticity[17], i.e.

$$\boldsymbol{\sigma} = \boldsymbol{D} : \boldsymbol{\varepsilon} + \beta \boldsymbol{D} : \dot{\boldsymbol{\varepsilon}} \tag{2}$$

in which $\boldsymbol{D}$ is the fourth-order elastic tensor and $\boldsymbol{\varepsilon}$

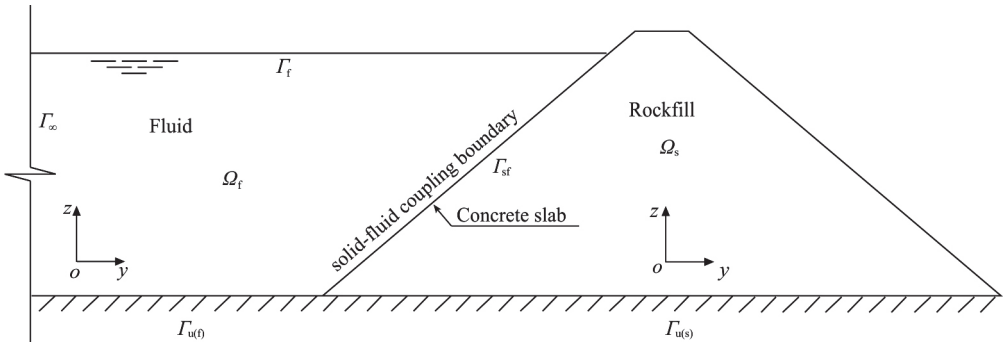

Fig. 1 The solid and fluid coupling system in a concrete face rockfill dam

the strain tensor, β is a constant reflecting the portion of the stress assumed by the dashpot that is paralleled to the elastic component.

The dynamic equilibrium equation for the fluid system can be similarly expressed as Eq. (1), however, the viscous force is generally neglected, i.e.

$$\rho_f \ddot{\boldsymbol{u}} + \nabla p = -\rho_f \ddot{\boldsymbol{u}}_g \tag{3}$$

where ρ_f is the fluid density, p the hydrodynamic pressure.

Applying the divergence operator $(\nabla\cdot)$ on both sides of Eq. (3) and neglecting the gradient of the fluid density, one can obtain the pressure based wave equation as follows

$$\rho_f \frac{\ddot{p}}{K_f} - \nabla^2 p = 0 \tag{4}$$

in which K_f is the linear bulk modulus of the fluid, i.e., $K_f = p/(-\nabla\cdot\boldsymbol{u}) = \ddot{p}/(-\nabla\cdot\ddot{\boldsymbol{u}})$.

For the solid (rockfill) system as depicted in Fig. 1, the boundary conditions of the relative displacement $\Gamma_{u(s)}$, velocity and acceleration can be specified as follows

$$\boldsymbol{u} = \dot{\boldsymbol{u}} = \ddot{\boldsymbol{u}} = \boldsymbol{0} \quad \text{on} \quad \Gamma_{u(s)} \tag{5}$$

and at the solid-fluid coupling boundary, Γ_{sf} the following condition holds

$$\boldsymbol{\sigma}\cdot\boldsymbol{n}_s = -\boldsymbol{p} = p\boldsymbol{n}_s \quad \text{on} \quad \Gamma_{sf} \tag{6}$$

in which $\boldsymbol{p}$ is the earthquake-induced traction exerted upon the concrete slabs and $\boldsymbol{n}_s$ the outer normal unit vector to the surface of the solid system.

Three kinds of boundary conditions are possible for the fluid system. At the solid-fluid coupling boundary including the base of the reservoir, Γ_{sf}, $\Gamma_{u(f)}$, Eq. (3) can be rewritten as follows

$$\nabla p = -\rho_f(\ddot{\boldsymbol{u}} + \ddot{\boldsymbol{u}}_g) \quad \text{on} \quad \Gamma_{sf} \cup \Gamma_{u(f)} \tag{7}$$

and at the free surface Γ_f, no hydrodynamic pressure will be present throughout an earthquake if the surface gravity wave is not considered, i.e.

$$p = 0 \quad \text{on} \quad \Gamma_f \tag{8}$$

In addition, the following equation can be used to represent the radiation of the pressure waves at the truncated boundary of the fluid domain (Γ_∞) [2]

$$\frac{\partial p}{\partial n} + \frac{1}{\sqrt{K_f/\rho_f}}\frac{\partial p}{\partial t} = 0 \quad \text{on} \quad \Gamma_\infty \tag{9}$$

in which $c_f = \sqrt{K_f/\rho_f}$ is the velocity of the pressure wave and $\partial p/\partial n = \boldsymbol{n}_f\cdot\nabla p$, where $\boldsymbol{n}_f$ should be interpreted as the outer normal unit vector to the fluid boundary surface.

The initial conditions of the solid-fluid coupling system are relatively simple, i.e.

$$\boldsymbol{u}(t=0) = \boldsymbol{0} \quad \text{in} \quad \Omega_s \tag{10a}$$

$$p(t=0) = 0 \quad \text{in} \quad \Omega_f \tag{10b}$$

Equations (1)-(10) can be solved numerically after the equivalent algebraic equations are obtained using the theory of the finite element method.

1.2 *Discretized equilibrium equations for the coupled system*

The weak form of Eq. (1) can be derived by introducing an arbitrary test function, $\boldsymbol{w}$, i.e.

$$\int_{\Omega_s} \boldsymbol{w}\cdot(\rho_s\ddot{\boldsymbol{u}} + \alpha\rho_s\dot{\boldsymbol{u}} + \nabla\cdot\boldsymbol{\sigma})\mathrm{d}v = \int_{\Omega_s} \boldsymbol{w}\cdot(-\rho_s\ddot{\boldsymbol{u}}_g)\mathrm{d}v,$$

$$\forall \boldsymbol{w} \in \boldsymbol{C}_1(\Omega_s) \tag{11}$$

In view of mathematical operations, the first derivative of the test function $\boldsymbol{w}$ is always assumed to be continuous within the solid domain, Ω_s. Implementing the standard Galerkin-weighted residual procedure to Eq. (11), one can obtain the following algebraic equations

$$\boldsymbol{M}_s\ddot{\boldsymbol{U}} + \boldsymbol{C}_s\dot{\boldsymbol{U}} + \boldsymbol{K}_s\boldsymbol{U} = -\boldsymbol{M}_s\ddot{\boldsymbol{U}}_g + \int_{\Gamma_{sf}} \boldsymbol{N}_s{}^T \boldsymbol{p}\mathrm{d}\boldsymbol{S} \tag{12}$$

in which $\boldsymbol{N}_s$ is the shape (interpolation) function for the displacement field. The uppercase displacement $(\boldsymbol{U})$, velocity $(\dot{\boldsymbol{U}})$ and acceleration $(\ddot{\boldsymbol{U}})$ should be seen as the nodal variables. The mass matrix $(\boldsymbol{M}_s)$, the stiffness matrix $(\boldsymbol{K}_s)$ and the damping matrix $(\boldsymbol{C}_s)$ can be expressed as follows

$$\boldsymbol{M}_s = \int_{\Omega_s} \boldsymbol{N}_s{}^T \rho_s \boldsymbol{N}_s \mathrm{d}v, \quad \boldsymbol{K}_s = \int_{\Omega_s} \boldsymbol{B}_s{}^T \boldsymbol{D}\boldsymbol{B}_s \mathrm{d}v,$$

$$\boldsymbol{C}_s = \int_{\Omega_s} \alpha \boldsymbol{N}_s{}^T \rho_s \boldsymbol{N}_s + \beta \boldsymbol{B}_s{}^T \boldsymbol{D}\boldsymbol{B}_s \mathrm{d}v = \alpha \boldsymbol{M}_s + \beta \boldsymbol{K}_s \tag{13}$$

in which the displacement-strain matrix $\boldsymbol{B}_s$ reads

$$\boldsymbol{B}_s = -\begin{pmatrix} \frac{\partial}{\partial x} & 0 & 0 \\ 0 & \frac{\partial}{\partial y} & 0 \\ 0 & 0 & \frac{\partial}{\partial z} \\ \frac{\partial}{\partial y} & \frac{\partial}{\partial x} & 0 \\ 0 & \frac{\partial}{\partial z} & \frac{\partial}{\partial y} \\ \frac{\partial}{\partial z} & 0 & \frac{\partial}{\partial x} \end{pmatrix} \boldsymbol{N}_s \tag{14}$$

The negative sign in Eq. (14) is due to the fact that the compressive strain is defined positive in this study. Note that the mass proportional damping $\alpha\boldsymbol{M}_s$ and the stiffness proportional damping $\beta\boldsymbol{K}_s$ in Eq. (13) are the results of introducing a velocity proportional damping force in Eq. (1) and using a viscoelastic constitutive model in Eq. (2). Both coefficients are often evaluated using the damping ratio (λ) of the dam materials[18-19]: $\alpha = \lambda\omega_1$, $\beta = \lambda/\omega_1$, in which ω_1 is the fundamental frequency of the structure.

The weak form of Eq. (4) can be similarly obtained by introducing an arbitrary continuous scalar function, w, within the fluid domain Ω_f, i.e.

$$\int_{\Omega_f} w\left(\rho_f \frac{\ddot{p}}{K_f} - \nabla^2 p\right)\mathrm{d}v = 0, \quad \forall w \in C_1(\Omega_f) \tag{15}$$

After applying the standard Galerkin-weighted residual procedure, Eq. (15) can be expressed similarly by an equivalent algebraic equation

$$\boldsymbol{M}_f\ddot{\boldsymbol{P}} + \boldsymbol{C}_f\dot{\boldsymbol{P}} + \boldsymbol{K}_f\boldsymbol{P} = -\int_{\Gamma_{sf}+\Gamma_{u(f)}} \rho_f \boldsymbol{N}_f{}^T \boldsymbol{n}_f \boldsymbol{N}_s \mathrm{d}\boldsymbol{S}(\ddot{\boldsymbol{U}} + \ddot{\boldsymbol{U}}_g) \tag{16}$$

in which $\boldsymbol{N}_f$ is the shape function for the pressure field. The uppercase pressure $(\boldsymbol{P})$ and its time derivatives ($\dot{\boldsymbol{P}}$, $\ddot{\boldsymbol{P}}$) are also the nodal variables. The mass matrix $(\boldsymbol{M}_f)$, the stiffness matrix $(\boldsymbol{K}_f)$ and the damping matrix $(\boldsymbol{C}_f)$ of the fluid system can be expressed as follows:

$$\boldsymbol{M}_f = \int_{\Omega_f} \boldsymbol{N}_f{}^T \frac{\rho_f}{K_f} \boldsymbol{N}_f \mathrm{d}v, \quad \boldsymbol{K}_f = \int_{\Omega_f} \boldsymbol{B}_f{}^T \boldsymbol{B}_f \mathrm{d}v,$$

$$\boldsymbol{C}_f = \int_{\Gamma_\infty} \boldsymbol{N}_f{}^T \frac{1}{\sqrt{K_f/\rho_f}} \boldsymbol{N}_f \mathrm{d}S \tag{17}$$

in which the gradient matrix $(\boldsymbol{B}_f)$ reads

$$\boldsymbol{B}_f = \begin{pmatrix} \frac{\partial}{\partial x} \\ \frac{\partial}{\partial y} \\ \frac{\partial}{\partial z} \end{pmatrix} \boldsymbol{N}_f \tag{18}$$

It should be pointed out that the water is assumed inviscous throughout the paper, and the damping term in Eq. (16) is a result of using Eq. (9) for the truncated boundary of the reservoir water. Eq. (12) and Eq. (16) are fully coupled because of the existence of the solid-fluid coupling terms related to the contacting boundary (Γ_{sf}).

1.3 *Solution strategies*

To solve the solid-fluid coupling equations, Eq. (12) is now rewritten as follows:

$$\boldsymbol{M}_{\mathrm{s}}\ddot{\boldsymbol{U}}+\boldsymbol{C}_{\mathrm{s}}\dot{\boldsymbol{U}}+\boldsymbol{K}_{\mathrm{s}}\boldsymbol{U}+\boldsymbol{S}_{\mathrm{sf}}\boldsymbol{P}=\boldsymbol{F}_{\mathrm{s}} \tag{19}$$

in which

$$\boldsymbol{F}_{\mathrm{s}}=-\boldsymbol{M}_{\mathrm{s}}\ddot{\boldsymbol{U}}_{\mathrm{g}},\quad \boldsymbol{S}_{\mathrm{sf}}=\int_{\Gamma_{\mathrm{sf}}}\boldsymbol{N}_{\mathrm{s}}^{\mathrm{T}}\boldsymbol{n}_{\mathrm{s}}\boldsymbol{N}_{\mathrm{f}}\mathrm{d}\boldsymbol{S} \tag{20}$$

Equation (16) can also be rewritten in a compacted form, i.e.

$$\boldsymbol{M}_{\mathrm{f}}\ddot{\boldsymbol{P}}+\boldsymbol{C}_{\mathrm{f}}\dot{\boldsymbol{P}}+\boldsymbol{K}_{\mathrm{f}}\boldsymbol{P}+\boldsymbol{S}_{\mathrm{fs}}\ddot{\boldsymbol{U}}=\boldsymbol{F}_{\mathrm{f}} \tag{21}$$

in which

$$\boldsymbol{F}_{\mathrm{f}}=-\boldsymbol{S}_{\mathrm{fs}}\ddot{\boldsymbol{U}}_{\mathrm{g}},\quad \boldsymbol{S}_{\mathrm{fs}}=\int_{\Gamma_{\mathrm{sf}}}\rho_{\mathrm{f}}\boldsymbol{N}_{\mathrm{f}}^{\mathrm{T}}\boldsymbol{n}_{\mathrm{f}}\boldsymbol{N}_{\mathrm{s}}\mathrm{d}\boldsymbol{S} \tag{22}$$

Note $\boldsymbol{F}_{\mathrm{f}}$ in Eq. (22) includes the contribution made by the reservoir base boundary $(\Gamma_{\mathrm{u(f)}})$. In view of the fact that $\boldsymbol{n}_{\mathrm{s}}=-\boldsymbol{n}_{\mathrm{f}}$ at the solid-fluid coupling boundary, the relationship between the two coupling matrixes, $\boldsymbol{S}_{\mathrm{sf}}$, $\boldsymbol{S}_{\mathrm{fs}}$, in Eqs. (20), (22) can be expressed as follows

$$\boldsymbol{S}_{\mathrm{sf}}=-\frac{1}{\rho_{\mathrm{f}}}\boldsymbol{S}_{\mathrm{fs}}^{\mathrm{T}} \tag{23}$$

Equations (19), (21) can be solved in the time domain using the Newmark's scheme[2, 6], i.e.

$$\ddot{\boldsymbol{U}}_{i+1}=\frac{1}{b\Delta t^2}(\boldsymbol{U}_{i+1}-\boldsymbol{U}_i)-\frac{1}{b\Delta t}\dot{\boldsymbol{U}}_i-\left(\frac{1}{2b}-1\right)\ddot{\boldsymbol{U}}_i,$$

$$\dot{\boldsymbol{U}}_{i+1}=\frac{a}{b\Delta t}(\boldsymbol{U}_{i+1}-\boldsymbol{U}_i)+\left(1-\frac{a}{b}\right)\dot{\boldsymbol{U}}_i+\left(1-\frac{a}{2b}\right)\Delta t\ddot{\boldsymbol{U}}_i \tag{24}$$

and

$$\ddot{\boldsymbol{P}}_{i+1}=\frac{1}{b\Delta t^2}(\boldsymbol{P}_{i+1}-\boldsymbol{P}_i)-\frac{1}{b\Delta t}\dot{\boldsymbol{P}}_i-\left(\frac{1}{2b}-1\right)\ddot{\boldsymbol{P}}_i,$$

$$\dot{\boldsymbol{P}}_{i+1}=\frac{a}{b\Delta t}(\boldsymbol{P}_{i+1}-\boldsymbol{P}_i)+\left(1-\frac{a}{b}\right)\dot{\boldsymbol{P}}_i+\left(1-\frac{a}{2b}\right)\Delta t\ddot{\boldsymbol{P}}_i \tag{25}$$

Herein a and b are two constants. Substituting Eqs. (24) and (25) into Eqs. (19) and (21) yields the iterative schemes for the latter two equations, i.e.

$$\left(\frac{1}{b\Delta t^2}\boldsymbol{M}_{\mathrm{s}}+\frac{a}{b\Delta t}\boldsymbol{C}_{\mathrm{s}}+\boldsymbol{K}_{\mathrm{s}}\right)\boldsymbol{U}_{i+1}-\frac{1}{\rho_{\mathrm{f}}}\boldsymbol{S}_{\mathrm{fs}}^{\mathrm{T}}\boldsymbol{P}_{i+1}=\tilde{\boldsymbol{F}}_{\mathrm{s},i+1} \tag{26}$$

$$\left(\frac{1}{b\Delta t^2}\boldsymbol{M}_{\mathrm{f}}+\frac{a}{b\Delta t}\boldsymbol{C}_{\mathrm{f}}+\boldsymbol{K}_{\mathrm{f}}\right)\boldsymbol{P}_{i+1}+\frac{1}{b\Delta t^2}\boldsymbol{S}_{\mathrm{fs}}\boldsymbol{U}_{i+1}=\tilde{\boldsymbol{F}}_{\mathrm{f},i+1} \tag{27}$$

in which

$$\tilde{\boldsymbol{F}}_{\mathrm{s},i+1}=\boldsymbol{F}_{\mathrm{s},i+1}+\boldsymbol{M}_{\mathrm{s}}\left[\frac{1}{b\Delta t^2}\boldsymbol{U}_i+\frac{1}{b\Delta t}\dot{\boldsymbol{U}}_i+\left(\frac{1}{2b}-1\right)\ddot{\boldsymbol{U}}_i\right]+\boldsymbol{C}_{\mathrm{s}}\left[\frac{a}{b\Delta t}\boldsymbol{U}_i-\left(1-\frac{a}{b}\right)\dot{\boldsymbol{U}}_i-\left(1-\frac{a}{2b}\right)\Delta t\ddot{\boldsymbol{U}}_i\right] \tag{28}$$

and

$$\tilde{\boldsymbol{F}}_{\mathrm{f},i+1}=\boldsymbol{F}_{\mathrm{f},i+1}+\boldsymbol{M}_{\mathrm{f}}\left[\frac{1}{b\Delta t^2}\boldsymbol{P}_i+\frac{1}{b\Delta t}\dot{\boldsymbol{P}}_i+\left(\frac{1}{2b}-1\right)\ddot{\boldsymbol{P}}_i\right]+\boldsymbol{C}_{\mathrm{f}}\left[\frac{a}{b\Delta t}\boldsymbol{P}_i-\left(1-\frac{a}{b}\right)\dot{\boldsymbol{P}}_i-\left(1-\frac{a}{2b}\right)\Delta t\ddot{\boldsymbol{P}}_i\right]+\boldsymbol{S}_{\mathrm{fs}}\left[\frac{1}{b\Delta t^2}\boldsymbol{U}_i+\frac{1}{b\Delta t}\dot{\boldsymbol{U}}_i+\left(\frac{1}{2b}-1\right)\ddot{\boldsymbol{U}}_i\right] \tag{29}$$

Equations (26), (27) can be unified as follows

$$\begin{bmatrix}\tilde{\boldsymbol{K}}_{\mathrm{s}} & \tilde{\boldsymbol{S}}_{\mathrm{fs}}^{\mathrm{T}}\\ \tilde{\boldsymbol{S}}_{\mathrm{fs}} & \tilde{\boldsymbol{K}}_{\mathrm{f}}\end{bmatrix}\begin{pmatrix}\boldsymbol{U}_{i+1}\\ \boldsymbol{P}_{i+1}\end{pmatrix}=\begin{pmatrix}\tilde{\boldsymbol{F}}_{\mathrm{s},i+1}\\ -\dfrac{b\Delta t^2}{\rho_f}\cdot\tilde{\boldsymbol{F}}_{\mathrm{f},i+1}\end{pmatrix} \tag{30}$$

where

$$\tilde{\boldsymbol{K}}_{\mathrm{s}}=\frac{1}{b\Delta t^2}\boldsymbol{M}_{\mathrm{s}}+\frac{a}{b\Delta t}\boldsymbol{C}_{\mathrm{s}}+\boldsymbol{K}_{\mathrm{s}},\quad \tilde{\boldsymbol{S}}_{\mathrm{fs}}=-\frac{1}{\rho_{\mathrm{f}}}\tilde{\boldsymbol{S}}_{\mathrm{fs}},$$

$$\tilde{\boldsymbol{K}}_{\mathrm{f}}=-\frac{1}{\rho_{\mathrm{f}}}(\boldsymbol{M}_{\mathrm{f}}+a\Delta t\boldsymbol{C}_{\mathrm{f}}+b\Delta t^2\boldsymbol{K}_{\mathrm{f}})$$

A great advantage of Eq. (30) is the symmetry of the generalized stiffness matrix on the left hand side, which largely reduces the requirement of the memory and the computational cost.

2. Verification

A finite element program dynamic response analysis program for earth and rockfill structures (DRAPERS) was developed using the above derived formulations[18]. This procedure was used successfully in reproducing the observed behavior of the Zipingpu CFRD during the great Wenchuan earthquake[19]. Herein, two simple examples are used to verify the

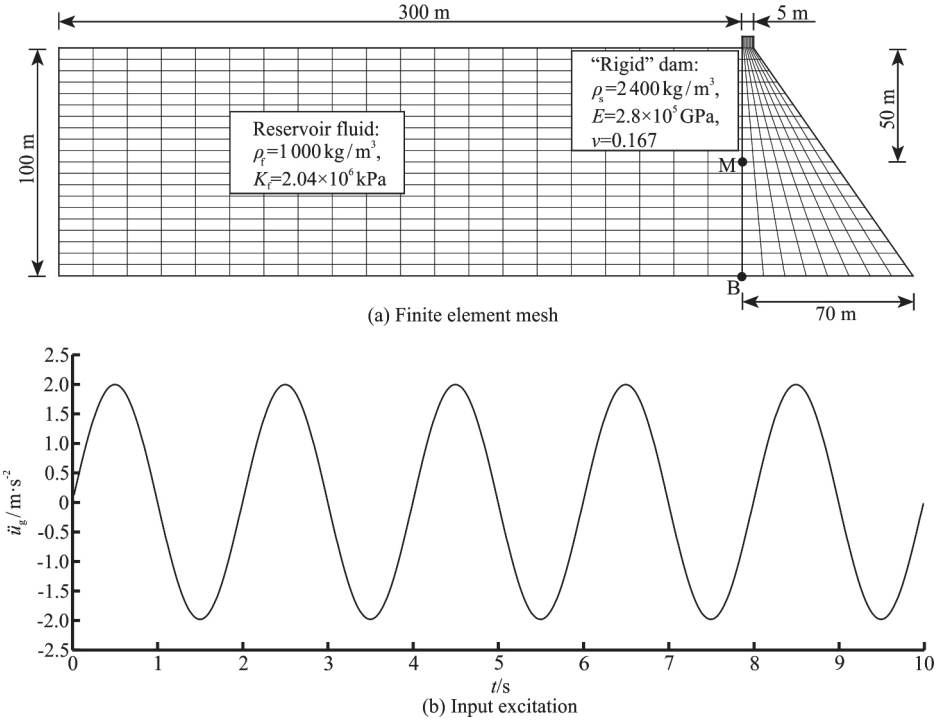

Fig. 2 The gravity dam and reservoir system and the input acceleration

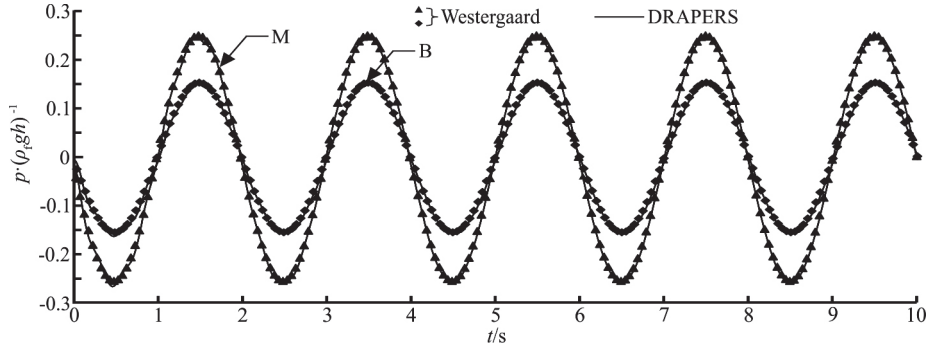

Fig. 3 Hydrodynamic pressures at the nodes M, B

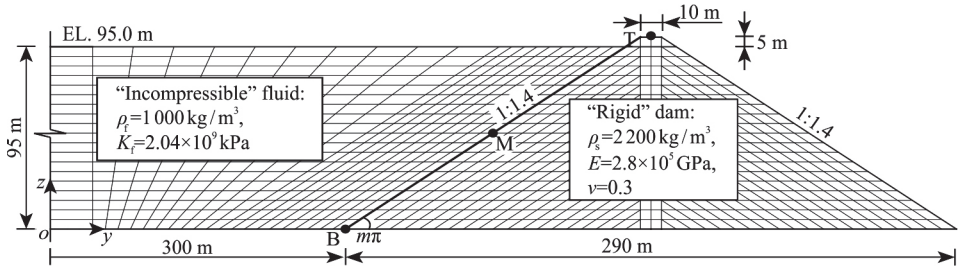

Fig. 4 Finite element mesh of the rockfill dam and reservoir system

above formulations and the program.

2.1 *A gravity dam with a vertical upstream surface*

A gravity dam with a vertical upstream surface is considered first. The solid-fluid coupling system is shown in Fig. 2(a). In order to use the analytical solution given by Westergaard, the gravity dam is assumed to be extremely rigid with an elastic modulus

of 2.8×10^5 GPa and a Poisson ratio of 0.167. The reservoir fluid has a density of 1 000 kg/m^3 and its bulk modulus is 2.04×10^6 kPa (corresponding to a pressure wave velocity of 1 430 m/s). Westergaard (1933) obtained the solution for the hydrodynamic pressure exerted upon a vertical rigid surface when it is subjected to a horizontal acceleration, i.e.

$$p(h)=-\ddot{u}_{\mathrm{g}}\frac{8\rho_{\mathrm{f}}H}{\pi^2}\sum_{n=1,3,5,\cdots,\infty}\frac{1}{n^2C_{\mathrm{n}}}\sin\left(\frac{n\pi}{2H}h\right) \tag{31}$$

in which

$$C_{\mathrm{n}}=\sqrt{1-\frac{16\rho_{\mathrm{f}}H^2}{n^2K_{\mathrm{f}}T_{\mathrm{g}}{}^2}} \tag{32}$$

where H is the depth of the reservoir and h the depth of a point measured from the free surface. T_{g} is the period of the harmonic excitation and $\ddot{u}_{\mathrm{g}}$ the ground acceleration. The negative sign in Eq. (31) indicates that a positive ground acceleration results in a negative hydrodynamic pressure because of the tendency of the fluid volume expansion due to the movement of the dam.

A sinusoidal acceleration excitation shown in Fig. 2(b) is input from the base of the dam, and the hydrodynamic pressure at two nodal points (M, B) are solved. Figure 3 compares the results predicted by DRAPERS and those by Eqs. (31), (32). It is clear that the numerical results agree almost exactly with the analytical solutions by Westergaard throughout the dynamic process.

2.2 *A rockfill dam with an inclined upstream surface*

A rockfill dam with an inclined upstream surface is considered. The ratio of both the upstream and downstream slope is 1:1.4, which is a convention in the modern CFRDs. The finite element meshes of this solid-fluid system is shown in Fig. 4. Chwang (1978) obtained the solution of such a coupling system based on the two-dimensional potential flow theory with the assumptions of a rigid dam and an incompressible fluid. The distribution of the hydrodynamic pressure reads

$$p(\xi)=-\ddot{u}_{\mathrm{g}}\rho_{\mathrm{f}}H\left[\frac{4}{\pi^2}\int_0^{\pi/2}\left(\frac{\xi}{\xi+\tan^2\theta}\right)^m\frac{\theta}{\sin\theta\cos\theta}\mathrm{d}\theta-\cot m\pi+\frac{\cos m\pi}{H}s(\xi)\right] \tag{33}$$

in which

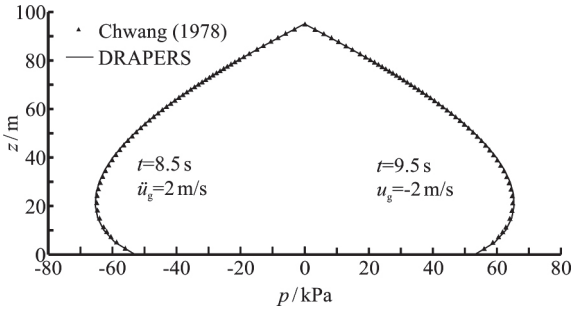

Fig. 5 Finite element mesh of the rockfill dam and reservoir system

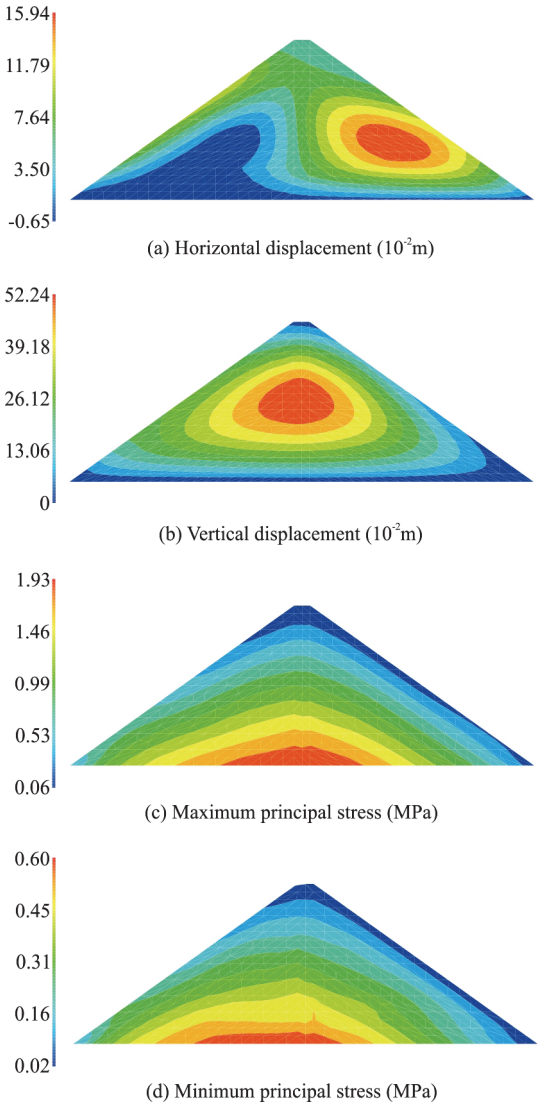

(a) Horizontal displacement (10^{-2}m)

(b) Vertical displacement (10^{-2}m)

(c) Maximum principal stress (MPa)

(d) Minimum principal stress (MPa)

Fig. 6 (Color online) Displacements and stress states of the dam prior to dynamic loading

$$s(\xi)=\frac{H}{\pi}\int_\xi^1\left(\frac{t}{1-t}\right)^m\frac{1}{t}\mathrm{d}t \tag{34}$$

is the distance of a point along the sloping surface measured from the base of the dam, where $m = 0.1974$ according to the slope ratio and the definition of this parameter, ξ is a variable ranging from 0 to 1, representing the water depth from 0 to H.

To be consistent with Chwang's assumptions, the rockfill dam, including the concrete slabs, are assumed to be extremely rigid with an elastic modulus of 2.8×10^5 GPa and a Poisson ratio of 0.30. The reservoir fluid has a density of 1 000 kg/m^3 and the bulk modulus is scaled up to 2.04×10^9 kPa. The acceleration shown in Fig. 2(b) is also used here as the base excitation. Figure 5 shows the hydrodynamic pressure distributions on the concrete slabs at two specific moments obtained analytically and numerically. Once again, both results agree with each other almost precisely. In addition, in both numerical and analytical results, the maximum pressure is predicted to be on a sloping dam at some distance above the dam base. This feature agrees quite well with the experimental findings obtained by the electric analog.

Excellent agreement between the numerical results and the corresponding exact solutions in the above two examples effectively confirms the reliability of the previously derived formulations and the finite element procedure. In the following parts, the hydrodynamic pressure on the CFRDs and the influential factors will be studied by numerical simulations. For the sake of simplicity, the finite element model shown in Fig. 4 will continue to be used, taking, however, the static and dynamic behaviors of the rockfill materials into account.

3. Several aspects in numerical simulations

3.1 *Initial condition of the dam*

It is well known that the dynamic behavior of the rockfill materials largely depends on the static stress states prior to the dynamic loading[13-14]. Therefore, establishing an authetic initial stress condition is an important prerequisite for the seismic analysis. In this study, the dam is assumed to be constructed layer by layer followed by one-stage casting of the concrete slabs and a gradual raise of the reservoir level. These processes are simulated in 30 steps using a hyperbolic constitutive model for the rockfill materials[20] and an isotropic elasticity model for the concrete slabs. The elastic modulus (E), the Poisson ratio (v) and the unit weight (γ) of the concrete are as follows:

$$E = 28\ \text{GPa},\quad v = 0.167,\quad \gamma = 24\ \text{kN/m}^3$$

The parameters for the rockfill materials are:

$$R_f = 0.75,\quad K = 1\,000,\quad n = 0.4,\quad K_b = 400,$$

$$m = 0.3,\quad \varphi_0 = 52°,\quad \Delta\varphi = 6°,\quad \gamma = 22\ \text{kN/m}^3$$

The physical meaning of these parameters can be found in the related literature[20]. The contours of the horizontal displacement and the settlement and those of the principal stresses are plotted in Fig. 6. Due to the hydrostatic pressure, almost the entire dam moves downstream with a maximum displacement of 159.4 mm. The maximum settlement predicted herein is 522.4 mm, accounting for about 0.5% of the dam height. Both the maximum and the minimum principal stresses are nearly proportional to the thickness of the overlying rockfill, with the maximum values of 1.93 MPa, 0.60 MPa at the bottom near the dam axis, respectively.

3.2 *Constitutive models for dynamic behavior*

The dynamic behavior of concrete slabs is also modeled by an elastic model, with the same parameters used in the previous static analysis. A damping ratio of 0.05 is adopted. The dynamic behavior of the rockfill materials is represented by a viscoelastic model[19], in which the equivalent shear modulus (G) and the damping ratio (λ) read:

$$G = k_1 p_a \left(\frac{p_0}{p_a}\right)^n \frac{1}{1+k_2\bar{\gamma}},\quad \lambda = \lambda_{\max}\frac{k_2\bar{\gamma}}{1+k_2\bar{\gamma}} \tag{35}$$

where k_1, k_2, n and $\lambda_{\max}$ are parameters, p_a is the atmospheric pressure used to normalize the initial mean effective stress (p_0). The normalized shear strain amplitude is defined as follows[19]

$$\bar{\gamma} = \frac{\sqrt{2}}{3}\frac{\sqrt{(\varepsilon_1-\varepsilon_2)^2+(\varepsilon_2-\varepsilon_3)^2+(\varepsilon_1-\varepsilon_3)^2}}{(p_0/p_a)^{1-n}} \tag{36}$$

The values of the involved parameters are given as follows:

$$k_1 = 2\,500,\quad k_2 = 40,\quad n = 0.35,\quad \lambda_{\max} = 0.20$$

They are all within the normal range of the compacted rockfill materials. The Poisson ratio of the rockfill materials is assumed to be 0.33.

It should be noted that the contact behavior between the concrete slabs and the underlying rockfill materials is not considered in the static and dynamic analyses. This idealization is adopted because the coupling effect on the surfaces of the concrete slabs is mainly due to the normal acceleration of this surface, and the tangential frictional behavior of the interface has not much contribution to the normal acceleration component. On the other hand, the inclusion of the

interface elements will inevitably increase the degree of nonlinearity and add the numerical difficulty for obtaining converged solutions[21-22]. Neglecting the pos- sible damage of the concrete slabs and their contacting behavior with the rockfill materials greatly simplifies the numerical simulations, without significant errors in the seismic response of the dam.

3.3 *Input accelerations*

Both regular and irregular acceleration histories are used in the following parts. The sinusoidal acceleration is adopted because of the convenience in studying the influence of the loading frequency. The acceleration is controlled by the amplitude and the period, i.e.

$$\ddot{u}_g(t) = \ddot{u}_{g,\max} \sin \frac{2\pi}{T_g} t \tag{37}$$

in which $\ddot{u}_{g,\max}$, T_g denote the acceleration amplitude and the period, respectively.

An irregular acceleration is also synthesized according to the designed response spectrum as shown in Fig. 7. This acceleration is used to study the hydrodynamic pressure on the hypothetic CFRDs subjected to a "real" earthquake.

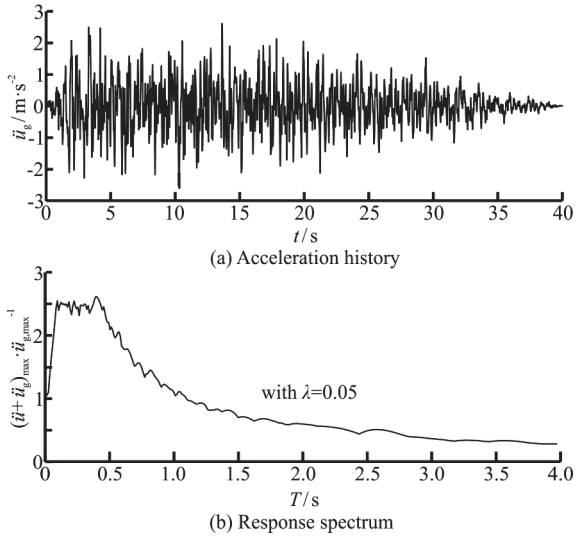

Fig. 7 Synthesized irregular acceleration history and the corresponding response spectrum

4. Results and interpretations

4.1 *Influence of excitation frequency*

A distinct dynamic feature of the rockfill dams is the dependence of the fundamental frequency of the free vibration upon the excitation as a result of the nonlinear dependence of the shear moduli of the rockfill materials on their shear strains (see Eq. (35)). Table 1 lists the fundamental frequency of the CFRD subjected to sinusoidal accelerations of a same amplitude of 2.0 m/s^2 but of four different periods. The fundamental frequency is obtained iteratively until the shear modulus of each element is compatible with its shear strain amplitude. The numerical scheme for the evaluation of the fundamental frequency of a coupled system is briefly described in the Appendix. In all four cases, neglecting the solid fluid coupling effect results in an overestimation of the fundamental frequency, no matter whether it is higher or lower than the excitation frequency. This can be explained easily in the light of the concept of the added mass of the fluid[2]. The fundamental frequency, on the other hand, is not evidently influenced by the compressibility of the fluid, i.e. an incompressible fluid assumption results in a negligible slightly lower frequency as shown in Table 1.

Figure 8 further compares the acceleration histories of the crest node T (Fig. 4) obtained with and without the solid fluid coupling effect. In the coupled simulations, the compressibility of the water is considered. Under the conditions of $T_g = 2$ s, 1.5 s and 0.5 s, no obvious deviation is observed in the obtained results. The difference of the acceleration histories, however, becomes most evident as the excitation period is reduced to 0.2 s. That is to say, the consequence of neglecting the hydrodynamic pressure on the CFRDs depends on the frequency content of the excitation. For those excitations abundant in high frequencies, neglecting the solid fluid coupling effect will result in an evident error in the acceleration response of the dam. This feature will be demonstrated again later.

4.2 *Influence of water compressibility*

The histories of the hydrodynamic pressure at two nodes, i.e., B, M (Fig. 4), obtained in the previous simulations using the sinusoidal accelerations are plotted in Fig. 9. We have two findings. First, although

Table 1 Frequency of the dam-reservoir system

Excitation		Fundamental frequency ω / rad·s^{-1}		
T_g /s	$2\pi \cdot / T_g^{-1}$ /rad·s^{-1}	No coupling	Coupled with compressible water	Coupled with incompressible water
2.0	3.14	8.42	8.06	8.04
1.5	4.19	8.30	7.90	7.89
0.5	12.56	8.14	7.84	7.82
0.2	31.42	9.24	8.94	8.91

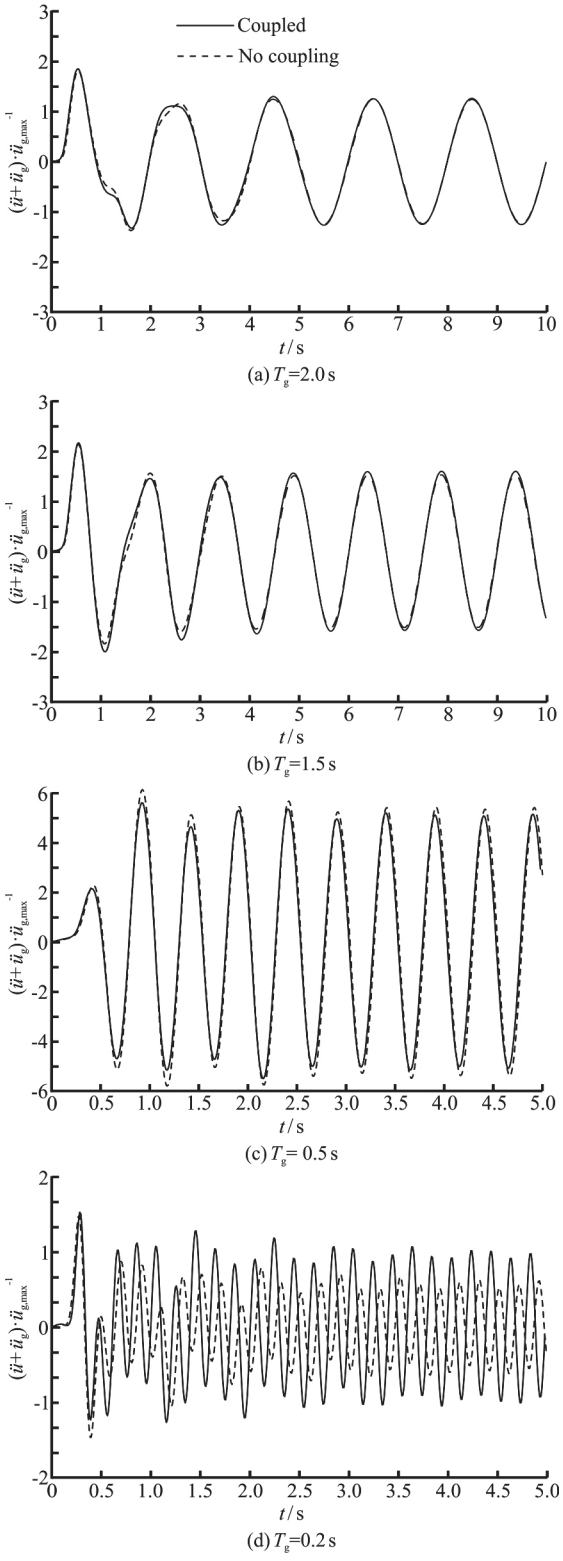

Fig. 8 Acceleration histories of node T excited by sinusoidal base accelerations

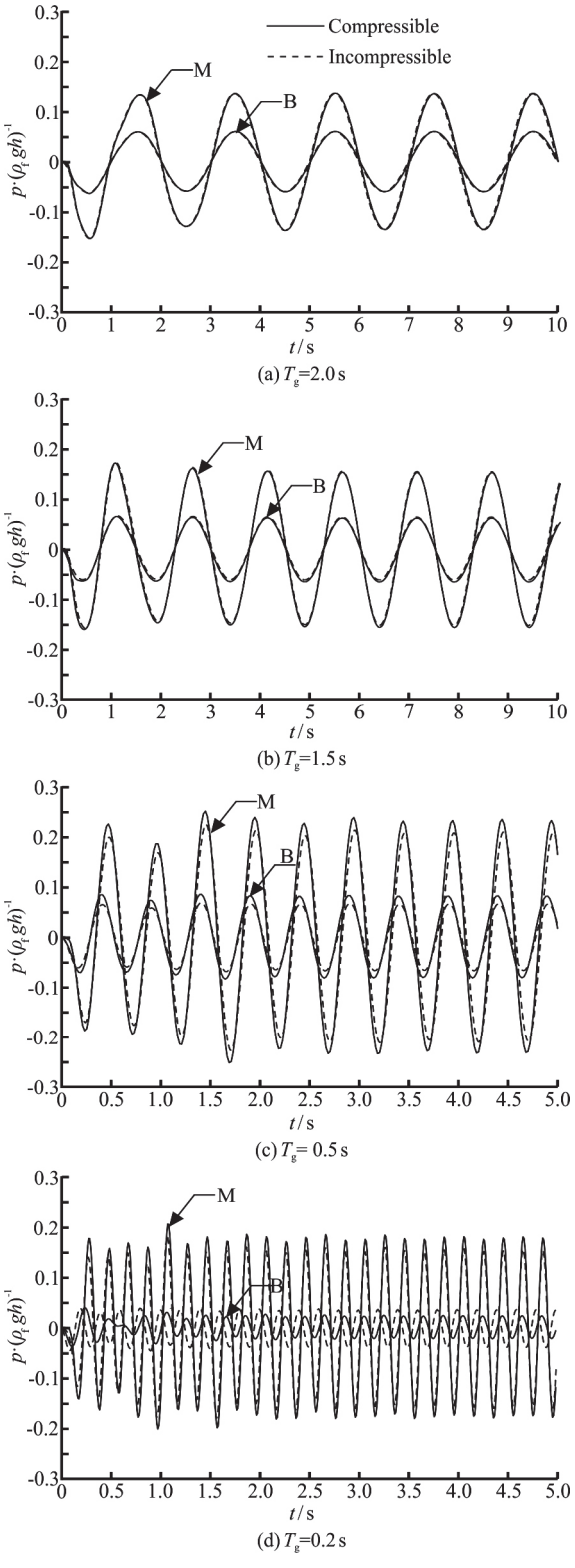

Fig. 9 Hydrodynamic pressures at nodes B, M excited by sinusoidal acceleration

although the peak acceleration of each excitation is the same, the maximum and minimum hydrodynamic pressures on the concrete slabs are not identical, i.e., they depend on the excitation frequency. For instance, the hydrodynamic pressures at nodes B and M are higher when $T_g = 0.5$ s than those in other cases.

This is due to the higher acceleration response of the dam (Fig. 8). Second, the compressibility of the fluid has almost no influence on the hydrodynamic pressure when the loading frequency is lower than the fundamental frequency of the dam. The influence of the fluid compressibility, however, becomes appreciable when the loading frequency is increased, particularly when it is considerably higher than the fundamental frequency of the dam as shown in Fig. 9(d).

Chopra (1968) suggested that the compressibility of the water has an insignificant effect on the earthquake excited dam response if its fundamental frequency is less than half of the first reservoir resonance. Taylor (1981) expressed this criterion as follows:

$$\omega_1 < \frac{\pi}{4}\frac{c_f}{H} = \frac{\pi}{4}\frac{\sqrt{K_f/\rho_f}}{H} \tag{38}$$

in which H denotes the water depth in the reservoir and ω_1 is the fundamental frequency of the dam. Herein, the fundamental frequency of the reservoir obtained numerically is about 24.09 rad/s, while the theoretical value given by Eq. (38) is 23.64 rad/s. If we compare both values with the fundamental frequency of the dam given in Table 1, we can find that the above criterion can always be satisfied. That is to say, an incompressible fluid assumption can be used safely in the seismic response analysis of the CFRD (100 m high) in this study. Fundamental frequencies of the CFRDs of six different heights, i.e., 50 m, 100 m, 150 m, 200 m, 250 m and 300 m are also studied with similar finite element meshes as shown in Fig. 4. Sensitivity analyses are conducted by changing the value of k_1 parameter that control the shear moduli of the dam materials (see Eq. (35)). In particular, $k_1 = 1\,500$ is adopted as the lower bound and $k_1 = 4\,000$ as the upper bound according to our experience. The dependence of the shear modulus upon the shear strain amplitude is not considered for simplicity. In this case, the fundamental frequencies of the dams are not influenced by the input excitation, as all dam materials have invariable shear moduli.

Figure 10 compares the minimum and maximum fundamental frequencies of the CFRDs obtained numerically and the threshold values predicted by Eq. (38). The relative locations of the bright and black circles and the threshold curve indicate the magnitude of the influence of the fluid compressibility. For example, the threshold values are generally over the possible range of the fundamental frequencies of the CFRDs lower than 100 m, meaning that the influence is negligible and the compressibility of the water can be safely neglected. On the other hand, the possibility of a fundamental frequency exceeding the threshold value increases evidently as the dam height increases. That is to say, the influence of the fluid compressibility will be more evident for the CFRDs higher than 100 m.

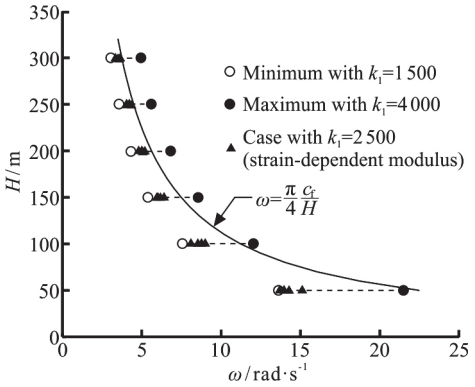

Fig. 10 Fundamental frequencies of CFRDs of different heights

It should be noted that the black circles in Fig. 10 correspond to the extremely rigid CFRDs since the degradation of the shear moduli of the rockfill materials with the shear strain amplitude is not considered. If this nonlinear stiffness behavior of the rockfill materials is taken into account, the natural frequency of the dam will be considerably reduced and the influence of the water compressibility on the seismic response will attenuate for the CFRDs higher than 100 m as will be shown later.

4.3 *Influence of vertical acceleration*

The slope of the CFRDs is much gentler than that of gravity dams or arch dams. Therefore, the hydrodynamic pressure caused by the vertical acceleration will be much more considerable in the CFRDs. Figure 11 shows the maximum and minimum hydrodynamic pressures (p_{max}, p_{min}) for different elevations caused by same sinusoidal acceleration histories ($\ddot{u}_{g,max}$ = 2.0 m/s^2) but specified to the vertical direction and the horizontal direction, respectively.

In all four cases, the hydrodynamic pressure caused by a vertical acceleration is higher than that induced by a horizontal one, especially when the excitation frequency is higher than the natural frequency of the dam. For instance, when the period of the ground excitation is 0.5 s, 0.2 s, the vertical acceleration induced hydrodynamic pressure at the base is almost twice of that induced by the horizontal acceleration, as shown in Fig. 11.

Another phenomenon that can be observed from Fig. 11 is the distribution of the maximum and minimum hydrodynamic pressures on the concrete slabs. With the increase of the loading frequency, the shape

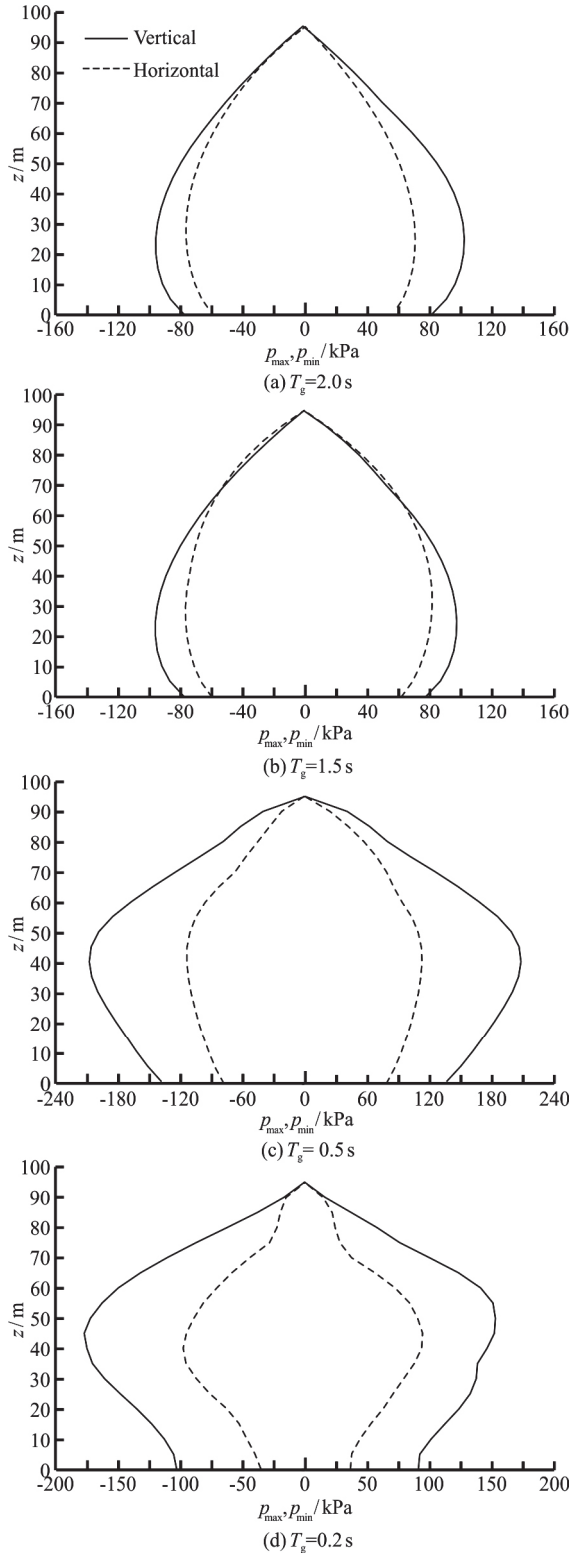

Fig. 11 Hydrodynamic pressures caused by vertical and horizontal accelerations

of the hydrodynamic pressure distribution changes and the place of the peak region moves upwards. The dependence of the hydrodynamic pressure distribution upon the loading frequency makes a single distribution function for the hydrodynamic pressure (such as the Westergaard's distribution or the Chwang's distribution) meaningless in a practical application. In addition, there is no similar analytical solution available for the evaluation of a vertical acceleration induced hydrodynamic pressure on sloping dams. Thus, coupled dynamic analyses are necessary for the CFRDs simultaneously excited by horizontal and vertical accelerations.

4.4 *Acceleration response of CFRDs*

The effects of the dam height and the vertical excitation were studied separately in the previous sections. Herein, the acceleration response of the CFRDs of different height, i.e., 50-300 m, are studied further. A horizontal acceleration shown in Fig. 7 as well as a vertical acceleration which is scaled down to 2/3 of the horizontal one, are specified to the base of the dams. Both coupled and uncoupled analyses are performed and the results are shown in Figs. 12, 13, respectively.

Clear discrepancies can be seen in the results obtained by coupled analyses and uncoupled analyses, for both the horizontal and vertical responses. In most cases, neglecting the solid fluid coupling effect leads to an overestimation of the acceleration amplification factors (AAFs) at the crest but meanwhile an underestimation of the AAFs within certain lower parts of the dams. In some cases the error caused by neglecting the coupling effect is rather considerable, as evident from the results shown in Figs. 12(b), 13(b). Therefore, the solid-fluid coupling effect is as much important as in the concrete dams. This conclusion based on the numerical results differs from that given by Bureau et al.[11]. Both Figs. 12, 13 also indicate that the values of the horizontal and vertical AAFs are much lower in higher CFRDs (200-300 m) than in lower dams (50-150 m). This trend can be explained by the lower fundamental frequency of higher CFRDs (Fig. 11) and thus a higher damping coefficient β in the Rayleigh damping matrix (Eq. (13)), as it is generally inversely proportional to the dam's fundamental frequency[16, 18].

Slight difference can be distinguished from the results obtained based on the assumptions of a compressible fluid and an incompressible fluid when the dam is higher than 100 m. However, when the dam is lower than 100 m, the effect of the water compressibility becomes negligible as the acceleration responses obtained under both conditions almost overlap each other. This is consistent with the finding as shown Fig. 10. In addition, the results shown in Figs. 12, 13 assure that the influence of the water compressibility on the acceleration response of the CFRDs lower than 300 m is negligible. This conclu-

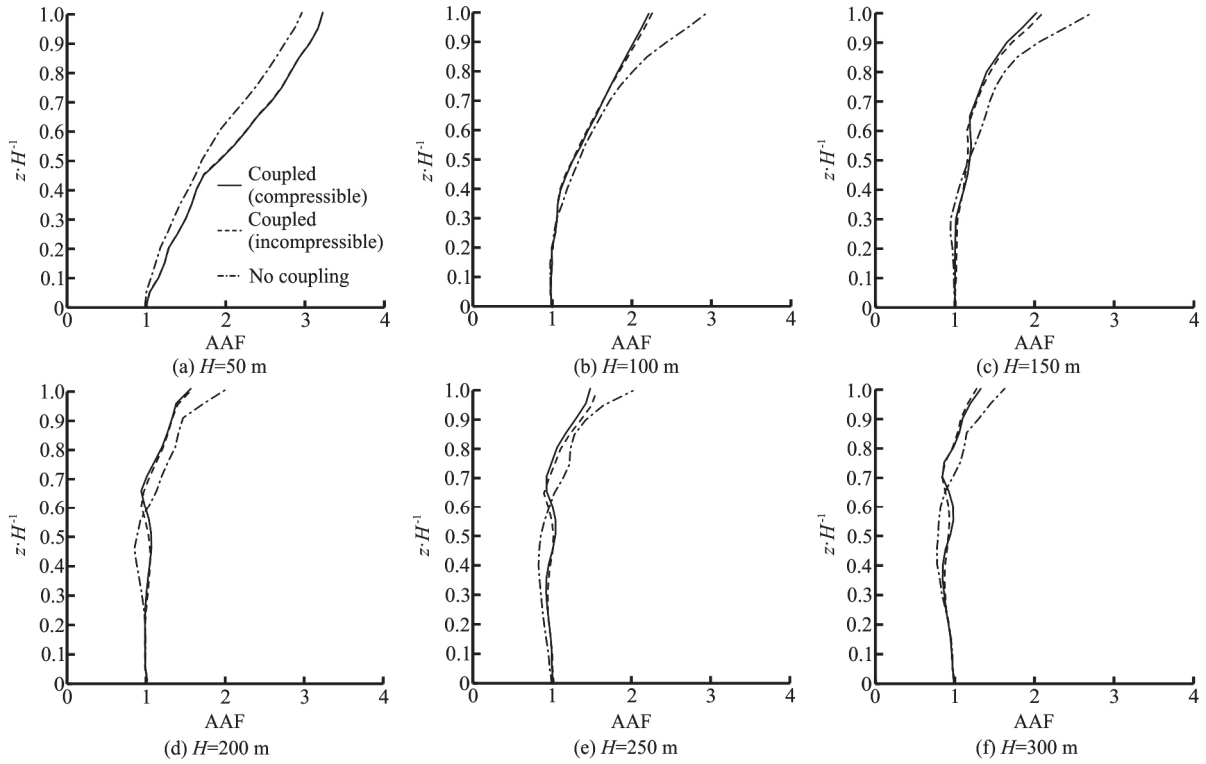

Fig. 12 Horizontal acceleration amplifications of CFRDs of different heights

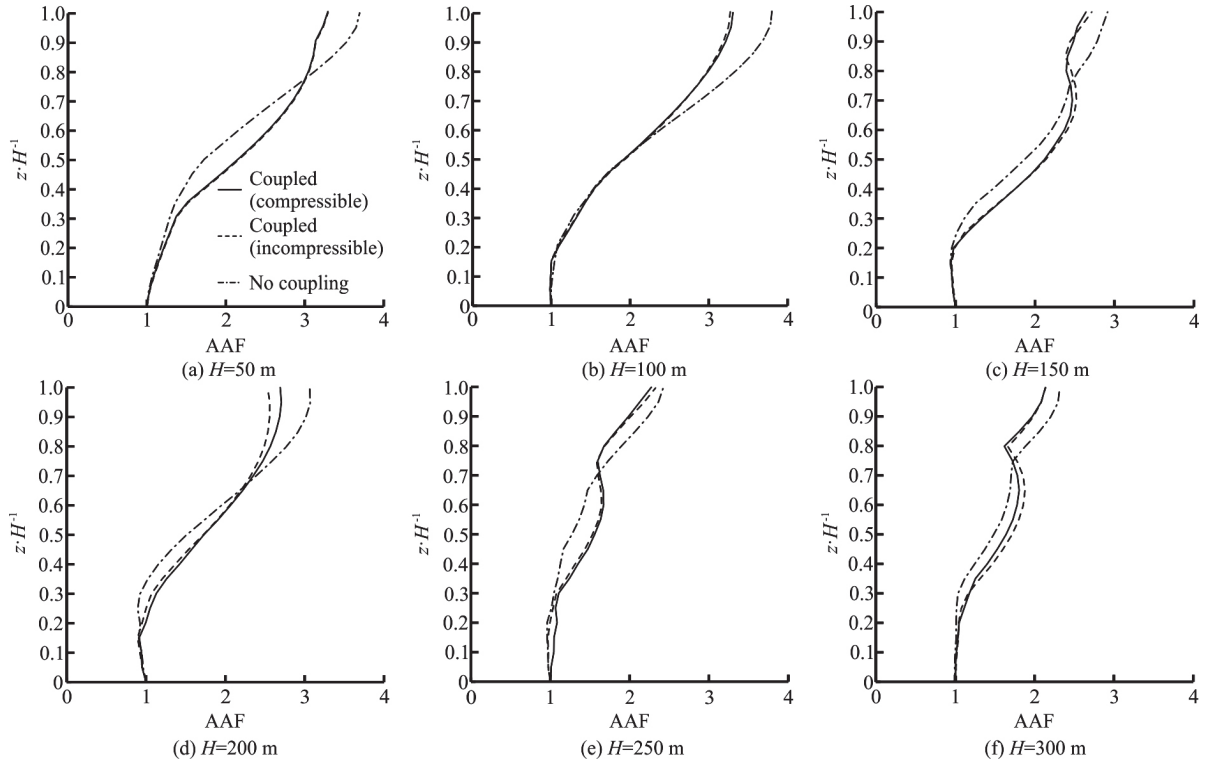

Fig. 13 Vertical acceleration amplifications of CFRDs of different heights

sion is further verified in Fig. 10 by comparing the fundamental frequencies of the dams (triangles) and the criterion given by Eq. (38). Note that the whole acceleration history is divided into 4 stages in the

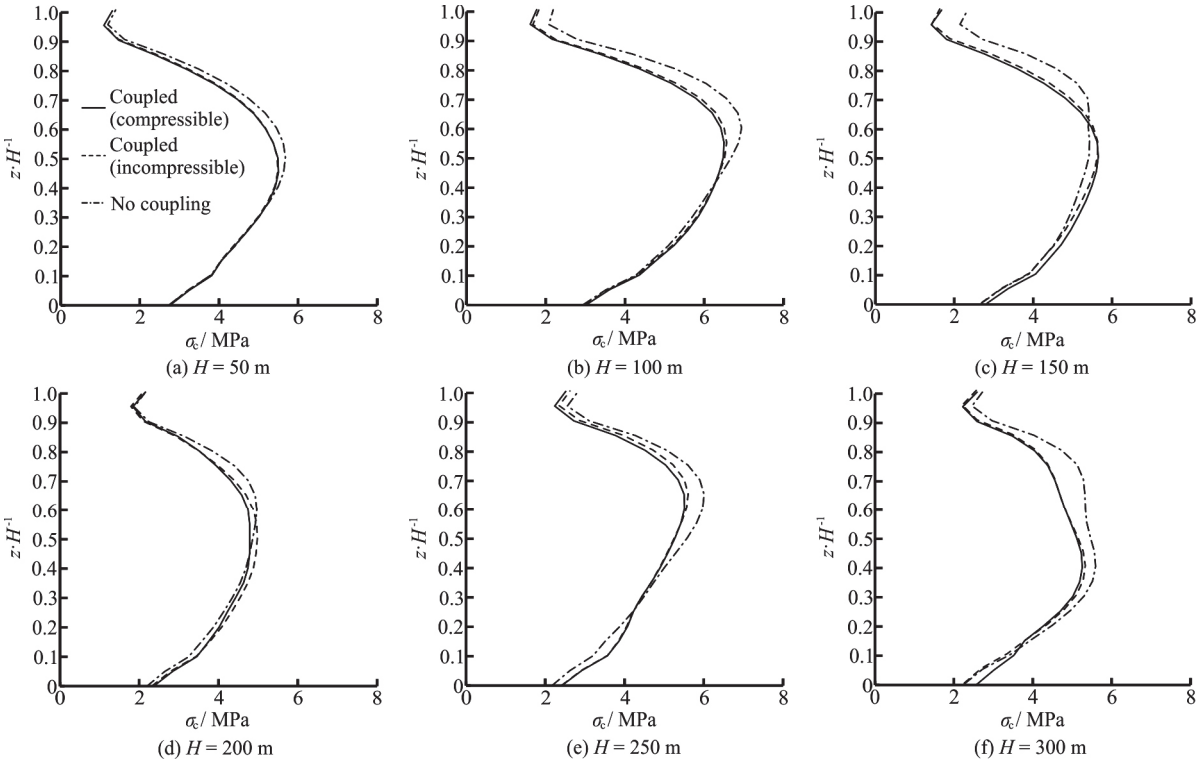

Fig. 14 Maximum compressive slope stresses in concrete slabs

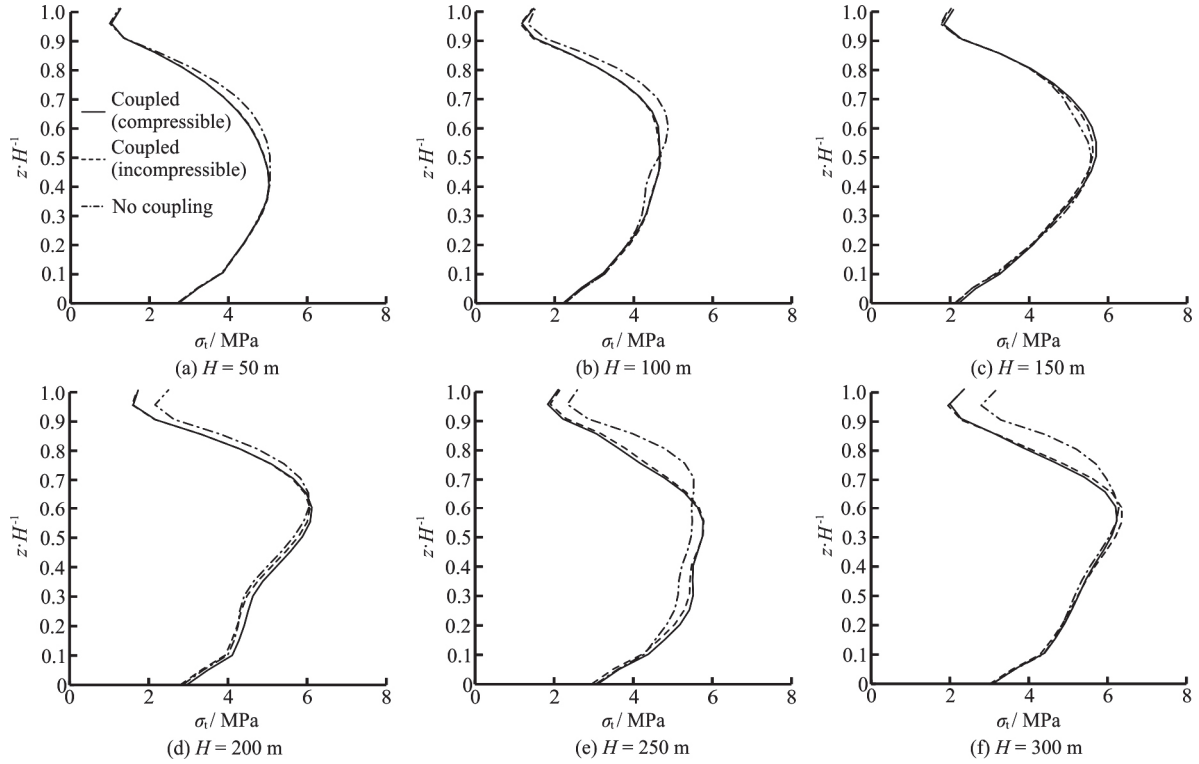

Fig. 15 Maximum tensile slope stresses in concrete slabs

equivalent linear dynamic analyses and different fundamental frequencies are obtained during each stage as shown in Fig. 10.

4.5 *Stress response of concrete slabs*

The distributions of the maximum normal com-

pressive stress and tensile stress at the water-retaining surfaces of the concrete slabs are plotted in Figs. 14, 15, respectively. These normal stresses are along the slope direction and the contributions of the gravity of the materials and the hydrostatic pressure are not included. They are obtained by averaging the dynamical stresses at the Gaussian integration points in slab elements. It can be seen that the regions of high dynamical stresses, both compressive and tensile ones, are near the center of the concrete slabs, no matter whether the solid fluid-coupling effect is taken into account or not. However, neglecting the coupling effect generally results in an overestimation of the maximum slope stresses within the upper half of the slabs, while the influence is less evident within the lower half of the concrete slabs. These numerical results rebukes the necessity of considering the hydrodynamic pressure in seismic response analyses of the CFRDs.

Comparison of the results shown in Figs. 14, 15 also confirms that the compressibility of the water does not influence the stress distribution within the concrete slabs significantly. That is to say, the well-known concept of added mass for an incompressible fluid can be used reliably in studying the seismic behavior of the CFRDs. This simplification can considerably reduce the computational cost since the added mass matrix can be obtained once for all and solely from the fluid system, and it can be used in the dynamic analysis of the solid system subsequently, i.e., the coupled governing equations can be solved in a decoupled manner. Otherwise, a step by step coupling analysis should be conducted, in which the number of degree of freedom is much larger than both the solid system and the fluid system.

5. Conclusions

This paper studies the factors that influence the hydrodynamic pressure on the concrete slabs and the necessity of conducting a solid-fluid coupling analysis in studying the seismic response of the CFRDs. The governing equations for the balance of the solid-fluid coupling system are revisited and the corresponding fully coupled equivalent finite element formulations are derived. The resultant algebraic equations have a symmetric stiffness matrix so that the memory requirement and the computational cost can be greatly reduced. The formulations are implemented in an equivalent linear dynamic analysis program developed for earth and rockfill dams, and the formulations and the program are verified by using analytical solutions of some simple hydrodynamic pressure problems. Various two-dimensional plane strain finite element simulations are then carried out for the hypothetical CFRDs subjected to regular and irregular acceleration excitations. The following conclusions are reached in this study:

(1) Neglecting the solid-fluid coupling effect generally results in an overestimation of the fundamental frequency of the dam-reservoir system. However, when the hydrodynamic pressure is considered, the compressibility of the reservoir water has almost no influence on the fundamental frequency.

(2) The compressibility of the reservoir water influences the hydrodynamic pressure on the concrete slabs and the acceleration response of the dam, the extent of which depends on the excitation frequency. Only when the excitation frequency is considerably higher than the fundamental frequency of the system will the influence of the water compressibility become evident. Therefore, for excitations abundant in high frequency contents, a coupled analysis with consideration of the water compressibility is necessary for the CFRDs.

(3) For the CFRDs lower than 100 m, the fundamental frequencies rarely reach the threshold values proposed by Chopra. With the increase of the dam height, the probability that the fundamental frequency exceeds the threshold increases, indicating that the influence of the water compressibility on the seismic response is increasingly evident. However, such influence is still negligible in most cases as evidenced by numerical simulations with consideration of the nonlinear material behavior.

(4) As a result of gentle upstream slopes of the modern CFRDs, a vertical excitation can generate considerable hydrodynamic pressure on the concrete slabs with magnitude generally higher than that caused by a same horizontal excitation. In addition, both the distribution of a vertical excitation induced hydrodynamic pressure and that of a horizontal acceleration induced one are closely related with the excitation frequency. Dependence of the hydrodynamic pressure on the excitation frequency and the existence of the vertical excitation make a coupled dynamic analysis necessary for a CFRD subjected to complex excitations.

(5) Neglecting the solid-fluid coupling effect in a CFRD with a height ranging from 50-300 m generally results in an overestimation of the acceleration response near the crest and also an overestimation of the dynamic stress within the upper half of the concrete slabs. Therefore, numerical simulations neglecting the hydrodynamic pressure yield conservative predictions, and for a reliable seismic analysis, the solid-fluid coupling effect should be considered. What is more, the influences of the water compressibility on the acceleration response of the dam and the dynamic stresses in the concrete slabs are slight and negligible. Thus, an incompressible fluid assumption is acceptable in seismic response analyses of the CFRDs even

when the dam is as high as 300 m.

Results presented in this paper also demonstrate what an economic and effective role that the numerical technique may play in a problem where a theoretical solution is difficult to obtain and an experimental investigation is also hard to perform. For instance, the compressibility of the water cannot be controlled easily and its influence on the hydrodynamic pressure cannot be studied experimentally. Numerical techniques serves as effective alternatives once they are verified.

Acknowledgement

This work was supported by the Ministry of Water Resource, China (Grant No. 201501035).

References

[1] Chen S. S., Han H. Q. Impact of the "5.12" Wenchuan earthquake on Zipingpu concrete face rock-fill dam and its analysis [J]. *Geomechanics and Geoengineering*, 2009, 4(4): 299-306.

[2] USACE (US Army Corps of Engineers). Time-history dynamic analysis of concrete hydraulic structures [C]. *Engineering Manual* (*EM 1110-2-6051*), Washington DC, USA, 2003.

[3] Liang Q., Chen K. C., Hou J. M. et al. Hydrodynamic modelling of flow impact on structures under extreme flow conditions [J]. *Journal of Hydrodynamics*, 2016, 28(2): 267-274.

[4] USACE (US Army Corps of Engineers). Arch dam design [C]. *Engineering Manual* (*EM 1110-2-2201*), Washington DC, USA, 1994.

[5] Chopra A. K. Earthquake analysis of arch dams: Factors to be considered [J]. *Journal of Structural Engineering*, 2012, 138(2): 205-214.

[6] Wang J. T., Zhang C. H., Jin F. Nonlinear earthquake analysis of high arch dam-water-foundation rock systems [J]. *Earthquake Engineering and Structural Dynamics*, 2012, 41(7): 1157-1176.

[7] Câmara R. J. A method for coupled arch dam-foundation-reservoir seismic behavior analysis [J]. *Earthquake Engineering and Structural Dynamics*, 2000, 29(4): 441-460.

[8] Chen B. F., Yuan Y. S. Hydrodynamic pressures on arch dam during earthquakes [J]. *Journal of Hydraulic Engineering, ASCE*, 2011, 137(1): 34-44.

[9] Fenves G., Vargas-Loli L. Nonlinear dynamic analysis of fluid-structure systems [J]. *Journal of Engineering Mechanics*, 1988, 114(2): 219-240.

[10] Du X. L., Wang J. T. Seismic response analysis of arch dam-water-rock foundation systems [J]. *Earthquake Engineering and Engineering Vibration*, 2004, 3(2): 283-291.

[11] Bureau G., Volpe R L., Roth W. et al. Seismic analysis of concrete face rockfill dams [C]. *Concrete Face Rockfill Dams–Design, Construction and Performance ASCE*, New York, USA, 1985, 479-508.

[12] Bayraktar A., Kartal M. E., Adanur S. The effect of concrete slab-rockfill interface behavior on the earthquake performance of a CFR dam [J]. *International Journal of Non-Linear Mechanics*, 2011, 46(1): 35-46.

[13] Uddin N. A dynamic analysis procedure for concrete-faced rockfill dams subjected to strong seismic excitation [J]. *Computers and Structures*, 1999, 72(1-3): 409-421.

[14] Kong X. J., Zhou Y., Zou D. G., et al. Numerical analysis of dislocations of the face slabs of the Zipingpu concrete faced rockfill dam during the Wenchuan earthquake [J]. *Earthquake Engineering and Engineering Vibration*, 2011, 10(4): 581-589.

[15] Dakoulas P. Nonlinear seismic response of tall concrete-faced rockfill dams in narrow canyons [J]. *Soil Dynamics and Earthquake Engineering*, 2012, 34(1): 11-24.

[16] Zou D. G., Xu B., Kong X. J. et al. Numerical simulation of the seismic response of the Zipingpu concrete face rockfill dam during the Wenchuan earthquake based on a generalized plasticity model [J]. *Computers and Geotechnics*, 2013, 49: 111-122.

[17] Ottosen N. S., Ristinmaa M. The mechanics of constitutive modeling [M]. London, UK: Elsevier, 2005.

[18] Fu Z. Z., Chen S. S., Wang T. B. Predicting the earthquake-induced permanent deformation of concrete face rockfill dams using the strain potential concept in the finite element method [J]. *International Journal of Geomechanics*, 2017, 17(11): 04017100.

[19] Chen S. S., Fu Z. Z., Wei K. M. et al. Seismic responses of high concrete face rockfill dams: A case study [J]. *Water Science and Engineering*, 2016, 9(3): 195-204.

[20] Yin Z. Z. Principles of Geotechnics [M]. Beijing, China: China Water Power Press, 2007(in Chinese).

[21] Zimmerman B. K., Ateshian G. A. A surface-to-surface finite element algorithm for large deformation frictional contact in febio [J]. *Journal of Biomechanical Engineering*, 2018, 140(8): 081013.

[22] Neto D. M., Oliveira M. C., Menezes L. F. Surface smoothing procedures in computational contact mechanics [J]. *Archives of Computational Methods in Engineering*, 2017, 24(1): 37-87.

Appendix

Dynamic analysis of a CFRD needs to specify a proper damping to the system. The most widely used one in practice is the so-called Rayleigh damping as given in Eq. (13), where two scalar factors (α, β) should be determined. In geotechnical engineering, both factors are related to the natural (particularly the fundamental) frequency of the system. Here we explain how to determine the fundamental frequency. To this end, Eqs. (19), (21), neglecting the damping terms and the excitation terms, are expressed as follows:

$$\begin{bmatrix} \boldsymbol{M}_{\mathrm{s}} & \boldsymbol{0} \\ \boldsymbol{S}_{\mathrm{fs}} & \boldsymbol{M}_{\mathrm{f}} \end{bmatrix} \begin{Bmatrix} \ddot{\boldsymbol{U}} \\ \ddot{\boldsymbol{P}} \end{Bmatrix} + \begin{bmatrix} \boldsymbol{K}_{\mathrm{s}} & -\dfrac{1}{\rho_{\mathrm{f}}} \boldsymbol{S}_{\mathrm{fs}}{}^{\mathrm{T}} \\ \boldsymbol{0} & \boldsymbol{K}_{\mathrm{f}} \end{bmatrix} \begin{Bmatrix} \boldsymbol{U} \\ \boldsymbol{P} \end{Bmatrix} = \begin{Bmatrix} \boldsymbol{0} \\ \boldsymbol{0} \end{Bmatrix} \tag{A1}$$

By using the following assumption

$$\begin{Bmatrix} \boldsymbol{U} \\ \boldsymbol{P} \end{Bmatrix} = \begin{Bmatrix} \boldsymbol{U}_0 \\ \boldsymbol{P}_0 \end{Bmatrix} \mathrm{e}^{\mathrm{i}\omega t} \tag{A2}$$

Equation (A1) can be rewritten as

$$\begin{bmatrix} \boldsymbol{K}_{\mathrm{s}} & -\dfrac{1}{\rho_{\mathrm{f}}}\boldsymbol{S}_{\mathrm{fs}}{}^{\mathrm{T}} \\ \boldsymbol{0} & \boldsymbol{K}_{\mathrm{f}} \end{bmatrix} \begin{Bmatrix} \boldsymbol{U}_0 \\ \boldsymbol{P}_0 \end{Bmatrix} = \omega^2 \begin{bmatrix} \boldsymbol{M}_{\mathrm{s}} & \boldsymbol{0} \\ \boldsymbol{S}_{\mathrm{fs}} & \boldsymbol{M}_{\mathrm{f}} \end{bmatrix} \begin{Bmatrix} \boldsymbol{U}_0 \\ \boldsymbol{P}_0 \end{Bmatrix} \tag{A3}$$

Since an asymmetric stiffness matrix in the left hand side is not convenient to be handled, Eq. (A3) is further rearranged to the following form

$$\frac{1}{\omega^2} \begin{Bmatrix} \boldsymbol{U}_0 \\ \boldsymbol{P}_0 \end{Bmatrix} = \begin{bmatrix} \boldsymbol{K}_{\mathrm{s}} & \boldsymbol{0} \\ \boldsymbol{0} & \boldsymbol{K}_{\mathrm{f}} \end{bmatrix}^{-1} \begin{bmatrix} \boldsymbol{M}_{\mathrm{s}} & \dfrac{1}{\rho_{\mathrm{f}}\omega^2}\boldsymbol{S}_{\mathrm{fs}}{}^{\mathrm{T}} \\ \boldsymbol{S}_{\mathrm{fs}} & \boldsymbol{M}_{\mathrm{f}} \end{bmatrix} \begin{Bmatrix} \boldsymbol{U}_0 \\ \boldsymbol{P}_0 \end{Bmatrix} \tag{A4}$$

Equation (A4) is the iterative form for the solution of the fundamental frequency and the corresponding eigenvector.